JOURNAL OF COMPUTATIONAL PHYSICS **147,** 86–113 (1998)
ARTICLE NO. CP986074

Modeling Viscoelastic Networks and Cell Deformation in the Context of the Immersed Boundary Method

Dean C. Bottino

Department of Mathematics, University of Utah, Salt Lake City, Utah 84112
E-mail: bottino@math.utah.edu

Received November 6, 1997; revised August 4, 1998

We present a straightforward numerical technique for modeling passive viscoelastic networks, such as the actin cytoskeleton of ameboid cells, in the context of the immersed boundary method. The technique involves modeling the cytoskeletal material as a network of dynamic elastic links immersed in the ambient cytosol. Linking rules of varying complexity allow the numerical network to exhibit varying degrees of viscosity, elasticity, shear thinning, and thixotropy (stress-overshoot). A series of simulated viscometer tests are used to analyze the mechanical properties of the model networks and the effects of input parameters on these properties. The numerical network is then used in the context of a full-cell model involving simulated micropipette aspiration. These micropipette aspiration tests indicate that the immersed boundary method—with the added enhancement of the viscoelastic network model presented here—can be developed into a versatile tool for studying the free-boundary deformations of passively stressed and actively moving ameboid cells.

Key Words: viscoelasticity; ameboid deformation; micropipette aspiration.

1. INTRODUCTION

Viscoelastic materials are ubiquitous in biology. In particular, cells rely on their viscoelastic cytoskeletons for mechanical strength and—in the case of *ameba proteus*, *dictyostelium discoideum*, human neutrophils, fibroblasts, and sarcoma cells—for active locomotion [1, 5, 16]. The immersed boundary method, developed by Peskin [17] to model blood flow in the heart, has been used to model other biological problems such as platelet aggregation [13], flagellar swimming [12, 11], and bacterial deposition [9]. The distinguishing feature of this method is that it can be used to model geometrically complex free-boundary structures as force fields immersed in a larger fluid domain.

In this paper we develop a numerical technique for modeling passive viscoelastic material in the context of the immersed boundary method, in order to expand the utility of

0021-9991/98 $25.00

Peskin's numerical method to a wider range of biological applications. The viscoelastic model consists of a network of elastic fibers in which the fiber nodes correspond roughly to the centers of entangled actin "islands." The mechanical properties of the network are governed by a set of linking rules that depend on distance, strain, and time. Many of the linking rule parameters, such as the time required to form a link between two proximate nodes, have straightforward biological interpretations. Numerical viscometer tests reveal the mechanical behavior of these networks, which are either viscoelastic fluids or solids, depending on the input parameter choices. Shear thinning behavior is also evident in the model networks. A network with appropriately chosen time-dependent linking rules exhibits solid/fluid duality depending on the duration of the applied stress, as well as behavior reminiscent of thixotropy; the effective viscosity of the ruptured model network increases with rest time after rupture. In the final section we present a numerical simulation involving the aspiration of a viscoelastic network-filled model cell into a micropipette.

1.1. Biological Background

The ameboid cell is supported by a cytoskeleton, which consists of a network of microtubules, intermediate filaments, and actin. While both microtubules and intermediate filaments contribute to the bulk rheology of ameboid cell cytoplasm, it is the active and passive remodeling of the actin cytoskeleton that is thought to be largely responsible for ameboid locomotion. Actin monomers polymerize to form elastic actin filaments, which in turn are joined by geometry-specific actin crosslinking proteins to form such structures as rodlike bundles, two-dimensional sheets, and three-dimensional gels [1]. We shall be interested mainly in the actin gel, which is found in the submembrane cortical layer as well as in the advancing pseudopodia of ameboid cells.

The rheology of actin gel has been studied both *in vitro* and *in vivo*. Cone-plate viscometer studies reveal that actin gel can be described as a viscoelastic fluid [5]. The four basic types of viscous, elastic, and viscoelastic materials are described in Fig. 1. When suddenly subjected to a constant shearing force, a viscoelastic fluid will deform with gradually diminishing shear rate. After a characteristic relaxation time, the elastic component of the viscoelastic fluid is completely loaded and the material continues to deform at a constant rate. When the load is removed, the elastic component of the material releases its stored energy, causing the material to rebound only partially back to its original configuration [3, 14].

Actin gel, however, is slightly more complicated than an idealized linear viscoelastic fluid. Actin gel appears to yield more easily to high stresses than to low stresses, a phenomenon referred to as shear thinning. Also, actin gel displays a time-dependent behavior referred to as thixotropy; the gel is stiff when deformed gently, but flows freely when under greater stress and becomes stiffer the longer it remains unstressed. One explanation for this phenomenon is that quiescent actin gel consists of interconnected "islands" of crosslinked actin, but under sufficient stress these islands break apart and slide past each other, providing little resistance to flow [15].

Micropipette aspiration studies have revealed more about the rheology of actin gel in a living cell. In these studies, ameboid cells such as the human neutrophil are aspirated partially into a micropipette with a diameter smaller than that of the cell. The distance into the pipette that the cell is drawn is measured as a function of time and aspiration pressure. Like the viscometer experiments, the micropipette experiments indicate that actin gel is viscoelastic. Furthermore, the cytoskeleton appears to be solid-like on

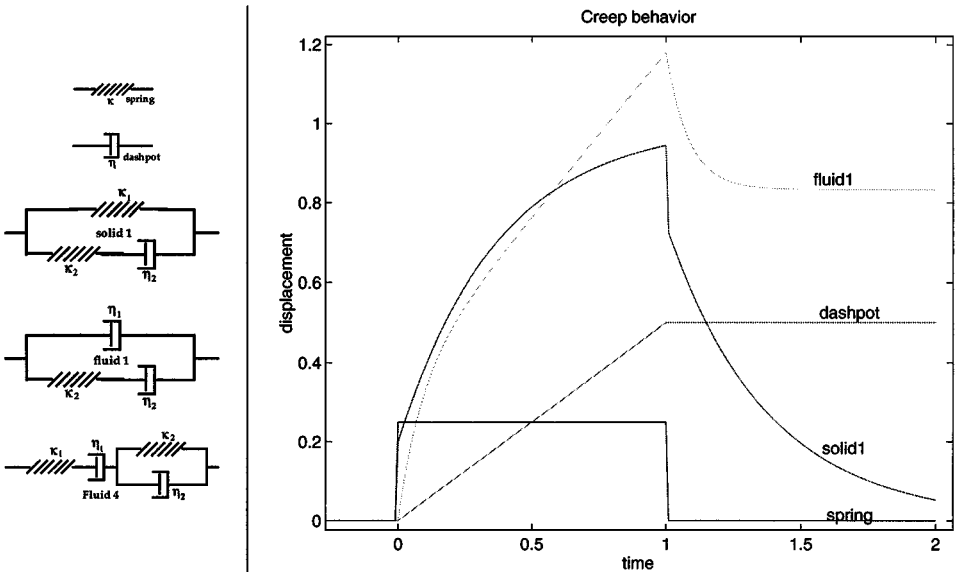

FIG. 1. Creep behavior of linear viscoelastic materials. The ideal elastic element ("spring") deforms instantaneously upon stress loading and returns to its original length instantaneously upon unloading. The ideal viscous element ("dashpot") deforms at a constant rate under loading and retains that deformation after unloading. A typical linear viscoelastic solid ("solid1") exhibits an initial instantaneous deformation at the instant of loading, followed by a dampened deformation toward some asymptotic strain. Upon unloading, the solid returns exponentially to its original configuration. A typical linear viscoelastic fluid ("fluid1") deforms at a diminishing rate which asymptotically approaches a constant deformation rate. Upon unloading, the fluid rebounds exponentially, but not all the way to its original configuration. More elaborate models, like "fluid4" (not plotted), can be constructed out of the basic viscous and elastic elements.

short timescales [22, 6] and more fluid-like, with the cell completely entering the pipette, on longer timescales [10]. The studies [22, 6] proceed to fit the analytically obtainable creep functions of linear viscoelastic materials to the deformation-versus-time data from living cells. The fitted parameters, however, vary with aspiration pressure—in particular, the parameters corresponding to the viscous elements in the linear models diminish with increasing aspiration pressure, indicating again that shear thinning is present. Further studies of this phenomenon indicate that the logarithm of the apparent viscosity of neutrophil cytoplasm decreases linearly with the log of the mean shear rate of cell entry into the pipette [23].

In Section 2 we present a mathematical model of actin network immersed in aqueous cytosol. Various rules for the linking dynamics among network nodes are presented. In Section 4.1, the effects of these linking rules on the mechanical properties of the network are tested by means of computational viscometer tests. These tests are used to determine the best-fitting linear viscoelastic model for each model network, as well as examining the shear thinning behavior and thixotropic properties of two of the model networks. The model networks are compared again in Section 4.2, this time in the context of the simulated micropipette aspiration of network-filled cells.

2. MATHEMATICAL FORMULATION

The actin cytoskeleton is modeled as a network of N_A points $\{\mathbf{A}_j\}_{j=1}^{N_A}$ with average spacing δA immersed in a two-dimensional domain Ω consisting of aqueous cytosol. The motion

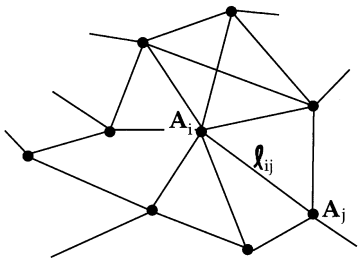

FIG. 2. Elastic interconnections among numerical actin nodes or "islands."

of the fluid phase is governed by the incompressible Navier–Stokes equations given by

$$\rho\left(\frac{\partial \mathbf{u}}{\partial t} + \mathbf{u}\cdot\nabla\mathbf{u}\right) = -\nabla p + \mu\Delta\mathbf{u} + \mathbf{F}, \tag{1}$$

$$\nabla\cdot\mathbf{u} = q(\mathbf{x}, t) \tag{2}$$

in Ω, with periodic boundary conditions on Ω. Equation (1) is Newton's second law, where ρ is the fluid density, μ is the viscosity, $\mathbf{u}$ is the fluid velocity, and $\mathbf{F}$ contains all of the forces transmitted by the network onto the fluid. In Eq. (2), $q(\mathbf{x}, t) \equiv 0$ implies incompressibility. In the micropipette test runs, which involve sources and sinks, we will have nonzero q on a vanishingly small subset of Ω; Eq. (1) is valid on the complement of this subset.

Recall that the cytoskeleton was described in the previous section as interconnected "islands" of crosslinked actin. Each network node $\mathbf{A}_j$ can therefore be thought of as the center of one of these islands, and the entanglements or interconnections between any two of these are then represented as elastic links ℓ_{ij} joining nodes $\mathbf{A}_i$ and $\mathbf{A}_j$. Figure 2 illustrates an example of such a network.

Let the position of node j at time t be denoted by $\mathbf{A}_j(t)$, or simply $\mathbf{A}_j$ if time dependence is understood. The network nodes move at the local fluid velocity. We express this as

$$\frac{d}{dt}\mathbf{A}_j = \mathbf{u}(\mathbf{A}_j, t). \tag{3}$$

As this network is carried along at the local fluid velocity, it may become strained from its original or "target" configuration, and as a result, the individual fibers in the network are strained from their target lengths. The dimensionless strain e_{ij} on a link ℓ_{ij} joining nodes $\mathbf{A}_i$ and $\mathbf{A}_j$ is given by

$$e_{ij} \equiv \frac{\|\mathbf{A}_i - \mathbf{A}_j\|}{\delta A_{ij}} - 1, \tag{4}$$

where δA_{ij} denotes the resting length of the link ℓ_{ij} joining the nodes. (It should be noted that in the limit as $\max_{ij}\delta A_{ij} \to 0$, the set of strains on the individual links characterize the Cauchy infinitesimal strain tensor for the material [14, 3].) The strain on a link results in tension on that link. If the interconnections between actin islands are assumed to act like Hookean springs up to rupture, then the tension T_{ij} of link ℓ_{ij} is a linear function of the strain, given by

$$T_{ij} \equiv S_{ij}e_{ij}, \tag{5}$$

where S_{ij} is the spring stiffness constant for the link ℓ_{ij} and e_{ij} is the strain as defined in (4).

In a general sense, (S_{ij}) and (δA_{ij}) can be thought of as sparse symmetric matrices that characterize the interactions between interacting nodes and, therefore, the mechanical behavior of the entire network. In this paper we will consider four types of networks with differing linking and forcing rules: the "control" network, the "memory" network, the "(capture) annulus" network, and the "time-dependent" network.

1. *Control network*. In this network, all the spring constants S_{ij} are set to zero, so that there is no linking and the only mechanical properties of the network/fluid composite are those of the ambient fluid.

2. *Memory network*. Proximate nodes at time $t = 0$ are joined for all time, with constant resting length and constant spring constants, regardless of the strains on the links. In terms of our mathematical formulation, we write this as

$$\begin{aligned} \delta A_{ij}(t) &= \|\mathbf{A}_i(0) - \mathbf{A}_j(0)\| \\ S_{ij}(t) &= S_{ij}(0) \end{aligned} \tag{6}$$

for all $t > 0$, where $S_{ij}(0) = S_A > 0$ if $r_{\min}\delta A < \|\mathbf{A}_i(0) - \mathbf{A}_j(0)\| < r_{\max}\delta A$, and $S_{ij}(0) = 0$ otherwise. In all of the memory network simulations in this paper, $r_{\min} = 0.8$ and $r_{\max} = 1.8$.

3. *Capture annulus network*. Let $r_{\min}\delta A$ and $r_{\max}\delta A$ denote the inner and outer radii of an annular region centered at a node $\mathbf{A}_j$. At each time t, the nodes $\mathbf{A}_j$ and $\mathbf{A}_i$ are linked by a spring with constant resting length δA and constant stiffness S_A as long as $r_{\min}\delta A < \|\mathbf{A}_i - \mathbf{A}_j\| < r_{\max}\delta A$, that is, as long as $\mathbf{A}_i$ is inside $\mathbf{A}_j$'s "capture annulus." This set of linking rules is intended to correspond to the tendency for inter-island connections to rupture under excessive tension and to fold easily under excessive compression. (See Fig. 3.)

4. *Time-dependent network*. Let t_{form} denote the time required for a link between two proximate nodes to form, and let t_{tot} denote the total age of the link, including formation time, before the link decays (disconnects). Let r_{rupt} denote the strain rupture ratio for the links, and let $r_{\min}\delta A$ and $r_{\max}\delta A$ be the inner and outer capture radii. Finally, let S_A be a constant elastic stiffness. The linking rules proceed as follows: for any node $\mathbf{A}_j$,

(a) If another node $\mathbf{A}_i$ enters the "capture annulus" around $\mathbf{A}_j$ at time $t = t_0$ and remains in that capture annulus for a duration of t_{form} seconds, then at time $t_1 = t_0 + t_{\text{form}}$ the nodes $\mathbf{A}_j$ and $\mathbf{A}_i$ are joined by a link ℓ_{ij} with resting length $\delta A_{ij} \equiv \|\mathbf{A}_i(t_1) - \mathbf{A}_j(t_1)\|$ and stiffness constant S_A.

(b) As soon as either (i) the strain ratio $e_{ij} + 1$ of link ℓ_{ij} exceeds the strain rupture threshold r_{rupt} **or** (ii) $t \geq t_0 + t_{\text{tot}}$, the link ℓ_{ij} is ruptured. If at this time $\mathbf{A}_i$ is still inside the capture annulus of $\mathbf{A}_j$ and it remains there for an additional time t_{form}, the link may reform with a new resting length, according to rule (a). See Fig. 3.

The time-dependent link formation criterion (4a) is intended to resemble the tendency of connections between separated islands of polymerized actin to reform, given sufficient time near each other (and thus sufficiently low shear rates). The link disruption criteria given in (4b) are supposed to capture the tendency of actin fibers to rupture under excessive strain as well as the continual remodeling process that the cytoskeleton undergoes in a living cell.

To determine the force density per unit area passed to the two-dimensional fluid domain by the internal network tension forces, we have to study the mechanical properties of the numerical network in the limit of spatial refinement, that is, as the characteristic node spacing distance $\delta A \to 0$. In this limit, the discrete actin points $\{\mathbf{A}_j\}$ become dense in a closed two-dimensional subregion A of Ω; thus for this discussion we consider the actin to

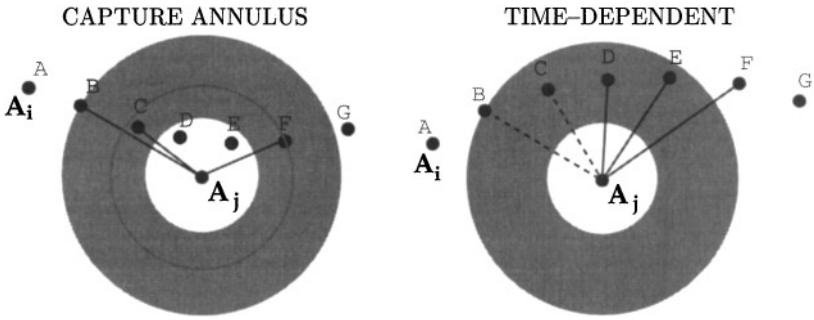

FIG. 3. Linking rules of the capture annulus and time-dependent networks. Under the **capture annulus** rules (left), the point $\mathbf{A}_i$ is not linked to the point $\mathbf{A}_j$ when it is at (A) since it is not in the shaded annular capture region of $\mathbf{A}_j$. As soon as $\mathbf{A}_i$ moves into the region it is immediately linked (B) to $\mathbf{A}_j$ by an elastic element of constant resting length δA (represented by darker circle inside shaded region). $\mathbf{A}_i$ remains linked as it passes through the region (C), but becomes unlinked upon exiting (D and E), linked again after reentering (F), and unlinked again at (G). Note that the link ℓ_{ij} between the points is under tension (B), compression (C), and is relaxed (F) at various points of its movement. Under the **time-dependent** linking rules, when the previously unlinked (A) point $\mathbf{A}_i$ enters the capture annulus of $\mathbf{A}_j$ at position (B) and remains (C) in the region until $t = t_1 \equiv t_0 + t_{\text{form}}$, then a link is established with resting length equal to the distance between the points at the moment they are linked (D). The link can persist even if $\mathbf{A}_i$ leaves the capture region (F) and will break (G) if the strain e_{ij} on the link exceeds the ratio r_{rupt} or if the link exceeds a certain age, that is, if $t > t_0 + t_{\text{tot}}$.

be a continuum material $\{\mathbf{A}(r, s) \mid (r, s) \in I_A \subset \mathbf{R}^2\}$ parameterized by the map $\mathbf{A} : I_A \to \Omega$. We determine the net force exerted by the surrounding network upon a small subset ΔA of the actin network parameterized by the rectangle $\Delta R = [r_1, r_2] \times [s_1, s_2]$ by summing the forces exerted on the four edges, or "faces," of its boundary:

$$\mathbf{F} = \int_{r_1}^{r_2} \mathbf{T}_s(r, s_2) - \mathbf{T}_s(r, s_1)\, dr + \int_{s_1}^{s_2} \mathbf{T}_r(r_2, s) - \mathbf{T}_r(r_1, s)\, ds. \tag{7}$$

Here $\mathbf{T}_s = \mathbf{n}_s \cdot \boldsymbol{\sigma} \|\partial \mathbf{A}/\partial r\|$ is the force per parametric element dr due to the stress tensor $\boldsymbol{\sigma}$ exerted on the edge of ΔA with outward normal $\mathbf{n}_s \equiv (\partial \mathbf{A}/\partial s)/\|\partial \mathbf{A}/\partial s\|$. The normalization factor $\|\partial \mathbf{A}/\partial r\|$ is needed because the two-dimensional stress tensor $\boldsymbol{\sigma}$ is measured in force per arc length. The interpretation of $\mathbf{T}_s$ in terms of the actin network is best stated as follows: the quantity

$$\int_{r_1}^{r_2} \mathbf{T}_s(r, s_2)\, dr \tag{8}$$

is the limit as $\delta A \to 0$ of the sum of the forces exerted upon the actin nodes inside ΔA by actin nodes outside ΔA via links passing through the s_2 "face" (given by $\{\mathbf{A}(r, s_2) \mid r \in [r_1, r_2]\}$) of ΔA (see Fig. 4).

By applying the fundamental theorem of calculus to (7), we establish the net force $\mathbf{F}$ on ΔA to be

$$\mathbf{F} = \int_{r_1}^{r_2}\int_{s_1}^{s_2} \frac{\partial}{\partial s}(\mathbf{T}_s)\, ds\, dr + \int_{s_1}^{s_2}\int_{r_1}^{r_2} \frac{\partial}{\partial r}(\mathbf{T}_r)\, dr\, ds = \int\int_{\Delta R} \frac{\partial}{\partial s}(\mathbf{T}_s) + \frac{\partial}{\partial r}(\mathbf{T}_r)\, dr^2. \tag{9}$$

Thus the force density per unit area of *parameter space* is given by

$$\mathbf{f} = \frac{\partial}{\partial s}(\mathbf{T}_s) + \frac{\partial}{\partial r}(\mathbf{T}_r) = \nabla \cdot \mathbf{T}, \tag{10}$$

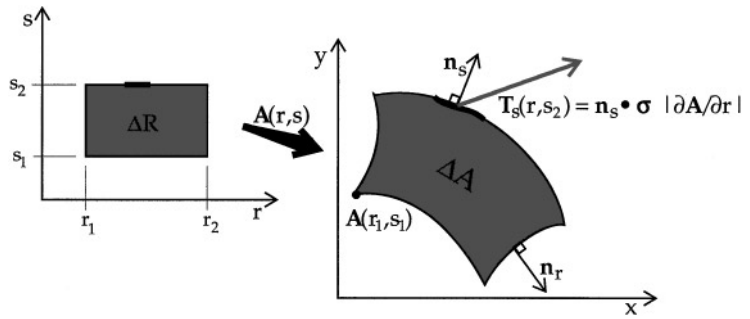

FIG. 4. An element $\Delta A = \mathbf{A}(\Delta R)$ of the actin continuum. The thickened segment on the upper face of ΔR is stretched by $\mathbf{A}(r, s)$ by a factor of $\|\partial \mathbf{A}/\partial r\|$, and $\mathbf{n}_s \cdot \sigma$ gives the force per unit length transmitted across the s_2 "face" of ΔA.

and the discretized force density, that is, the net force $\mathbf{f}_j$ on each node $\mathbf{A}_j$, is

$$\mathbf{f}_j = \frac{1}{\delta A} \sum_i T_{ij} \frac{\mathbf{A}_i - \mathbf{A}_j}{\|\mathbf{A}_i - \mathbf{A}_j\|}, \tag{11}$$

where δA ($\sim \Delta r \sim \Delta s$) is the spacing parameter (and in passive networks, resting length) for the actin network and T_{ij} is the tension in the link joining $\mathbf{A}_i$ and $\mathbf{A}_j$, determined according to one of the forcing rules discussed above. The force applied by the *discretized* structure onto the fluid is then found by setting $\Delta r = \Delta s = \delta A$ and using a discrete version of the integral in (9):

$$\mathbf{F}^n = \sum_{j=1}^{N_A} \mathbf{f}_j(t) \delta(\mathbf{A}_j(t) - \mathbf{x})(\delta A)^2, \tag{12}$$

where δ is the dirac delta function.

3. COMPUTATIONAL METHOD

In order to implement the above formulation numerically, we discretize both space and time. The square fluid domain $\Omega = [0, L] \times [0, L]$ is discretized as an $N_G \times N_G$ square grid with spacing $\Delta x = L/N_G$. The Navier–Stokes equations (1) are discretized as

$$\rho \left(\frac{\mathbf{u}^{n+1} - \mathbf{u}^n}{\Delta t} + \sum_{s=1}^{\eta} u_s^n D_s^{\pm} \mathbf{u}^n \right) = -\mathbf{D}^0 p^{n+1} + \mu \sum_{s=1}^{\eta} D_s^+ D_s^- \mathbf{u}^{n+1} + \mathbf{F}^n \tag{13}$$

$$\mathbf{D}^0 \cdot \mathbf{u}^{n+1} = q^n, \tag{14}$$

where $n = t/\Delta t$ denotes the timestep, D^+ is the forward difference operator, D^- is the backward difference, D^0 is the center difference, $\mathbf{D}^0 \cdot$ denotes discrete center difference divergence, $D_s^{\pm}$ is upwind difference (if $\sigma = \text{sign}(u_s)$ then $D_s^{\pm} \equiv D_s^{-\sigma}$), and η is the number of dimensions, in our case two [18]. This discretization is well-suited to the simulations that follow because the nonlinear velocity term is treated explicitly in time, allowing the parabolic viscosity term to be solved implicitly by fast Fourier transforms. The explicit treatment of the nonlinear term does not pose a stability problem in this case since the

simulations take place at a low Reynolds numbers ($\mathrm{Re} \sim 10^{-5}$). The explicit treatment of the force term $\mathbf{F}^n$ and the sink term q^n, however, requires that the time step Δt be sufficiently small to prevent numerical instability. While implicit forcing methods (using $\mathbf{F}^{n+1}$) have been used to stabilize the immersed boundary method for larger time steps, such an improvement has not yet been considered for this method.

Given $\mathbf{u}^n$ and $\{\mathbf{A}_i^n\}$, a single timestep of this simulation proceeds as follows:

1. The immersed points $\{\mathbf{A}_i^n\}$ are moved according to the interpolated local fluid velocity to compute $\{\mathbf{A}_i^{n+1}\}$ analogously to (3),

$$\mathbf{A}_i^{n+1} = \mathbf{A}_i^n + \Delta t \sum_{k,l=0}^{N_G - 1} \mathbf{u}_{kl}^n \, d\left(x_i^n - k\Delta x\right) d\left(y_i^n - l\Delta x\right)(\Delta x)^2, \tag{15}$$

where $\mathbf{A}_i^n = (x_i^n, y_i^n)$ and $d(r)$ is the discrete delta function originally used by Peskin in [17]:

$$d(r) = \begin{cases} \frac{1}{4\Delta x}\left(1 + \cos\left(\frac{\pi r}{2\Delta x}\right)\right), & |r| < 2\Delta x, \\ 0, & |r| \geq 2\Delta x. \end{cases} \tag{16}$$

2. The resulting strain on the links among the points is measured, and restoring forces $\mathbf{f}_i$ are assigned to all of the points according to (11) and (10).

3. Since the mass of the network is inherited from the ambient fluid, the internal network forces are transmitted directly to the surrounding fluid. The force $\mathbf{F}_{kl}^n$ at the finite-difference lattice node $(k\Delta x, l\Delta x)$ is computed by replacing the dirac delta function in (12) by the discrete delta function $d(r)$ given in (16):

$$\mathbf{F}_{kl} = \sum_{i=1}^{N_A} \mathbf{f}_i \, d(x_i - k\Delta x) \, d(y_i - l\Delta x)(\delta A)^2. \tag{17}$$

The $\mathbf{F}^n$ computed at each node in the discretized fluid domain is entered as the force term in the discretized Navier–Stokes equations (13).

4. If the pressure drop is being set in order to simulate micropipette aspiration, $q(\mathbf{x}, t)$ is updated and passed to the fluid grid in (14).

5. The discretized Navier–Stokes equations (13) and (14) are solved by a fast Fourier transform method to obtain $\mathbf{u}^{n+1}$. For details of the method used see [19, 18, or 4].

Note that one of the features of the immersed boundary method is that the mechanical properties of the immersed structures affect the fluid solver only in the explicit force term. This allows the modeling of complex immersed structures by use of fast fluid solvers on simple computational domains.

4. COMPUTATIONAL RESULTS

4.1. Wall Shear Experiments

In the complete ameboid locomotion model, the actin cytoskeletal network acts in conjunction with the cell membrane, transmembrane focal attachments, and the substratum in order to produce locomotion. The passive mechanical properties of the actin network alone are therefore difficult to measure in this context, so we have devised a computational experimental "apparatus" to test in isolation the actin network subject to the various forcing and linking rules presented in Section 2.

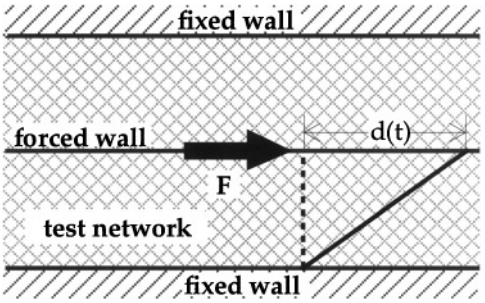

FIG. 5. Numerical apparatus for testing shear stress vs strain rate behavior of model actin network. The network–fluid composite occupies the space between the fixed walls, on both sides of the moving (forced) wall. The deformation $d(t)$ is determined by tracking the displacement of fluid markers from their original (dashed line) positions to their strained (solid line) configuration.

4.1.1. *Setup of Numerical Apparatus*

The apparatus, shown in Fig. 5, consists of two stationary immersed boundary walls flanking a movable immersed boundary wall. The numerical network occupies the space between the walls. The initial configuration of the actin nodes is established as follows; they are distributed in a regular hexagonal pattern with spacing of δA between nodes, then each node is displaced uniformly randomly from the hexagonal pattern with a maximum displacement of $0.75\ \delta A$. A horizontal shearing force F_s is applied to the wall and, in order to prevent the wall from deviating from its original plane $y = y_w$, it is constrained in the vertical direction.

Since the material on either side of the forced wall is identical, half of the shearing force F_s applied along the wall is transmitted to the material on each side. The stress tensor at any point immediately on either side of the wall is, therefore,

$$\boldsymbol{\sigma} = \begin{bmatrix} 0 & F_s/2L \\ F_s/2L & 0 \end{bmatrix}, \tag{18}$$

where L is the length of the walls. There is no variation in the x direction, so the strain tensor in the network simplifies to

$$\epsilon = \begin{bmatrix} \frac{\partial v}{\partial x} & \frac{\partial v}{\partial y} + \frac{\partial \omega}{\partial x} \\ \frac{\partial v}{\partial y} + \frac{\partial \omega}{\partial x} & \frac{\partial \omega}{\partial y} \end{bmatrix} = \begin{bmatrix} 0 & \frac{\partial v}{\partial y} \\ \frac{\partial v}{\partial y} & 0 \end{bmatrix}, \tag{19}$$

where (v, ω) gives the displacement field of the material. Thus if we measure the horizontal displacement $d(t)$ of a point in the stressed wall as a function of time, we can determine the mean strain and strain rate experienced by the material between the moving and fixed walls, reducing the experimental data to a single variable and simplifying the subsequent analysis.

In order to measure the behavior of the material in both the stressed and unstressed state, we use a time-dependent step-loading function of the form

$$F_s = F_0(H(t) - H(t - t_r)), \tag{20}$$

where F_0 is the force magnitude, H is the heaviside function, and t_r is the time of stress unloading.

We measure the "strain history" of the network by recording at regular time intervals the horizontal displacement $d(t)$ of a marker point initially located in the center of the moving

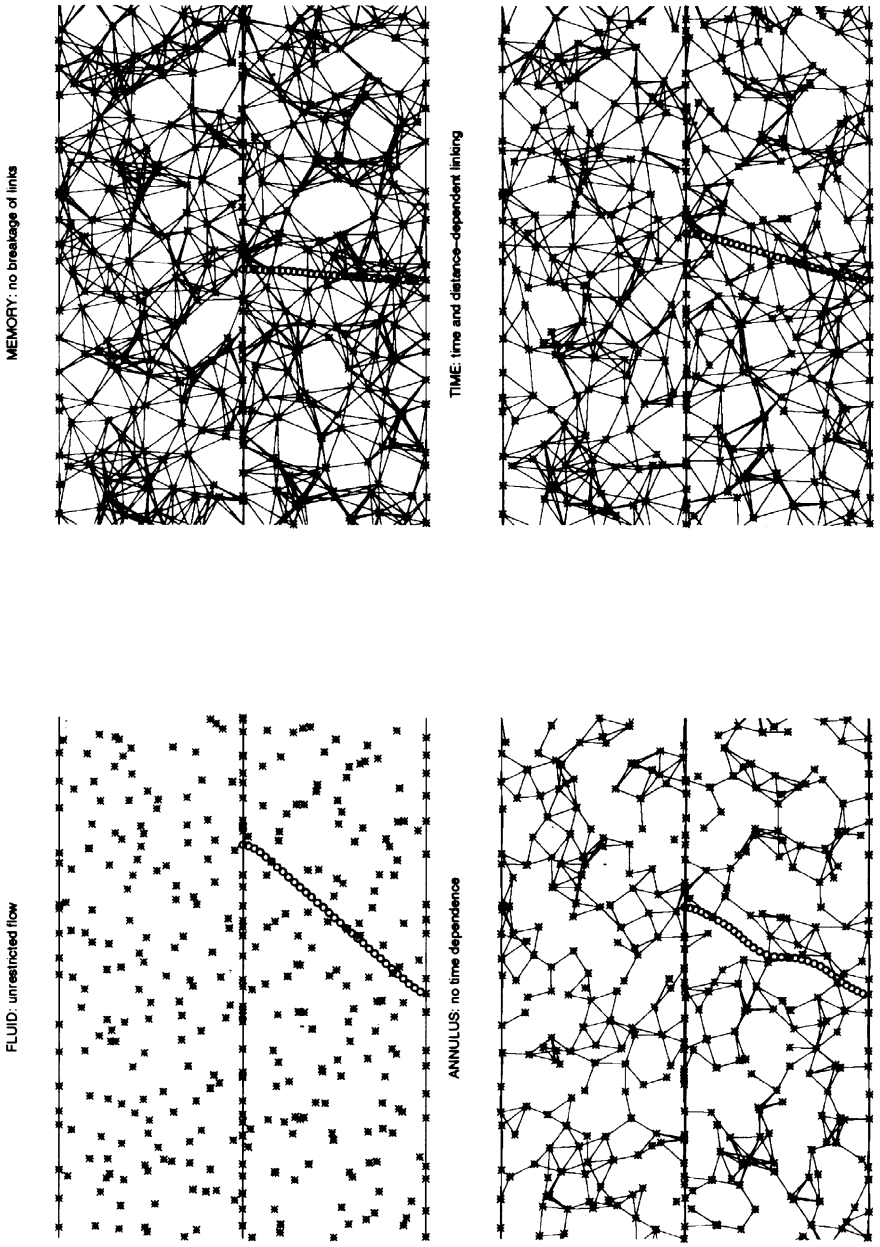

FIG. 6. Numerical network shear tests for various networks at the instant of stress unloading. The circular fluid markers are arranged perpendicularly to the walls at time $t = 0$.

wall. Snapshots of each run at time $t = t_r$ are shown in Fig. 6. All of the runs in this section were executed on a 64×64 fluid grid.

4.1.2. *Assessment of Mechanical Properties of Numerical Networks*

The qualitative mechanical behavior of the different types of numerical cytoskeletal networks was assessed by attempting to fit strain evolution curves of various mechanical

models to the strain data from the runs. The five nontrivial linear viscoelastic models we considered are shown in Fig. 1. For each model one can obtain a differential equation relating the force F, extension d, and rate of extension $\dot{d}$ for the system. We solved these equations for $d(t)$ subject to the prescribed force $F_s(t)$ given in (20) with $F_0/L = 0.01$ dyn/cm. This solution $d(t)$ is referred to as the *creep function for constant stress* for $t \leq t_r$ and the *creep function for the unloaded phase* of the material for $t > t_r$ [14, 3].

Next, we used the Levenberg–Marquardt method [21] to fit the model parameters to the data generated by each numerical experiment for $t \leq t_r$, that is, for the *loading phase only* of the simulation. These fitted values were then used to predict the unloading phase of the run in order to assess how well that model described the mechanical properties of that cytoskeletal network for that run. In other words, for each run, the model with the smallest "full merit function" (the sum of the squares of the error, taken over both loading and unloading phases) was considered to best describe the mechanical properties of the network. Since models with more parameters will in general be able to fit as well as or better than the models with fewer parameters, the model with the fewest parameters that described the data nearly as well as the models with more parameters was considered to be the simplest, most adequate description of the behavior of that network. The results of these tests are illustrated in Fig. 7.

The best-fitting model for the control run (fluid only) was the Maxwell element, which is a spring connected in series with a dashpot. The fitted spring constant κ was very high in this case, which was to be expected, since the limiting behavior of the Maxwell element as $\kappa \to \infty$ is that of a simple dashpot with viscosity η.

The memory network behavior was fit well by the Voigt model, which consists of a spring with stiffness κ linked in parallel to a dashpot with viscosity η. This is not surprising since the Voigt model is essentially a damped spring, corresponding to the numerical network springs damped by the viscous fluid in which the nodes are immersed.

Both the capture annulus and the time-dependent networks sheared easily as though they were fluid, and when the load was removed, they rebounded only slightly. This viscoelastic fluid behavior was best characterized by the three-element fluid model (Fluid1 in Fig. 1). For the capture annulus network, the fit over the unloading phase was much better in the low fiber stiffness case ($S_A = 0.24$) than in the higher stiffness case ($S_A = 0.48$); this may be evidence of the insufficiency of the linear models in describing the mechanical behavior of these numerical networks, which will be further explored in the next section.

It is interesting to note that during loading of the capture annulus and "time dependent" networks the velocity of the wall that shears this material (the slope of the graphed data points in Fig. 7) is nearly constant, and more importantly, is smaller than the velocity in the control. Thus the dynamic linking in these networks increases the effective viscosity (for this particular force magnitude) of the material between the plates.

A behavioral feature observed in living cytoplasm but not yet reproduced by this numerical model is an instantaneous initial deformation the moment that the stress is applied. Two mechanical models often used to describe the cytoskeleton, referred to in Fig. 1 as Solid1 [22] and Fluid4 [5], exhibit this behavior. The numerical model does not exhibit this instantaneous deformation because the movement of the network elements are necessarily damped by the ambient fluid in which they are immersed. This is the case in actual cytoskeleton as well; there is friction between the actin fibers and the cytosol. This apparent shortcoming of the numerical model might be overcome by increasing the force magnitude and spring stiffness constants relative to the ambient fluid viscosity. This has not yet been explored in detail,

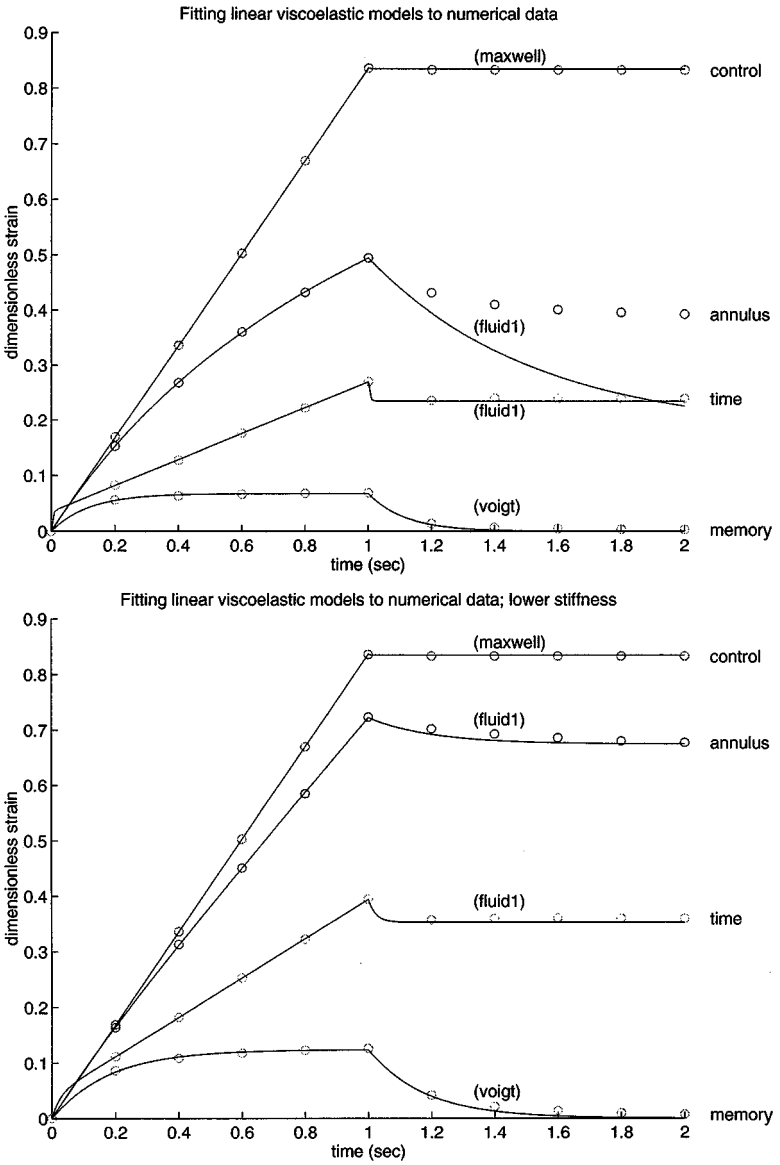

FIG. 7. Results of model fitting to data ouput from wall-shearing tests. Fitting results for network fiber stiffness constant $S_A = 0.48$ (top) and $S_A = 0.24$ (bottom). The curves were fitted only for the loading phase of the simulation, and the fitted values were then used to predict the unloading behavior for that run. The simplest linear viscoelastic model from Fig. 1 with the best fit to both loading and unloading phases is shown.

but comparison between the "Fluid1" curve fitted to the time-dependent network data for $S_A = 0.24$ and the curve fitted to the data from the same network for $S_A = 0.48$ would indicate that an instantaneous deformation-type behavior is indeed being approached with increasing fiber stiffness.

4.1.3. *Shear Thinning Behavior*

Unlike any of the linear viscoelastic models to which it has been compared, living cell cytoskeleton appears to exhibit a shear thinning behavior [23]; for example, in the

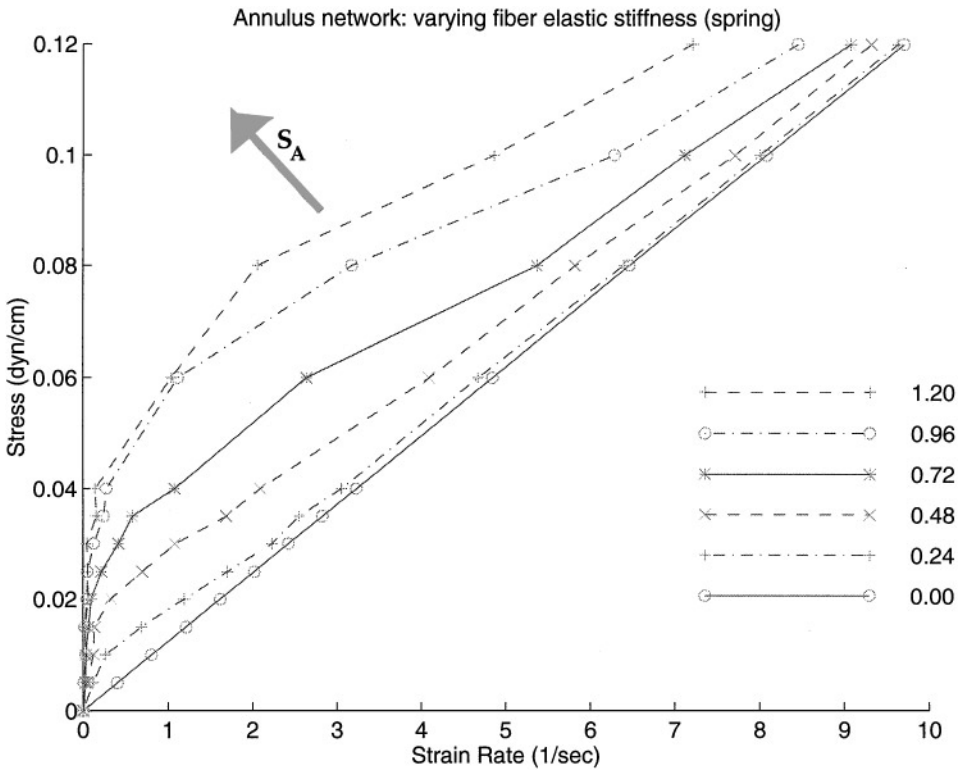

FIG. 8. Stress versus steady-state strain rate curves for capture annulus network. The steady-state viscosity of the network was tested for different values of the elastic link stiffness constant S_A, given in dynes.

micropipette studies described in [22], the dashpot viscosity obtained by fitting the aspiration distance data to the Solid1 model (see Fig. 1) is inversely proportional to the aspiration pressure that acted upon the cell. The following numerical studies indicate that both the capture annulus and time-dependent networks behave as shear thinning materials.

The stress σ versus strain rate $\dot{\epsilon}$ curves for each network were determined by subjecting each to a constant shearing force for sufficient time to ensure that a constant velocity was reached. The resulting $(\dot{\epsilon}, \sigma)$ coordinate was then plotted for various stress magnitudes. Furthermore, the numerical parameters for the networks were varied in order to observe the affects of those parameters on the rheology of the simulated materials.

Figure 8 illustrates the stress-strain rate relationships for the capture annulus network for various values of the elastic link stiffness S_A. The $S_A = 0$ case (unimpeded fluid) is included for comparison. Note that the network–fluid composite material behaves in a nonlinear (non-Newtonian) fashion for nonzero values of S_A; in particular, the capture annulus network exhibits shear thinning behavior. Not surprisingly, the material becomes "stiffer" as the stiffness S_A is increased. The numerical parameters of the capture annulus network, their effects on the rheology of the network–fluid composite, and their possible biophysical interpretations are summarized in Table I.

In Fig. 9 we observe the effect of S_A on the rheology of the time-dependent network. Once again, this network behaves like a shear thinning viscoelastic fluid and increasing S_A stiffens the network. The smoothness of the stress–strain rate curves for the time-dependent network suggests that this numerical network responds more predictably than the annulus

TABLE I
Numerical Parameters of the Capture Annulus Linking Rules

Parameter name	Default value	Rheological effect	Description; biological interpretation
S_A	0.48 dyn/cm	Stiffening	Stiffness constant; the aggregate stiffness of the actin filaments joining two islands of crosslinked actin.
r_{max}	1.8	Stiffening	Outer capture radius ratio; if set to equal to 1, the network will have only compressive forces. If increased, increases number of links at each node.
r_{min}	0.8	Relaxing	Inner capture radius ratio; if set equal to 1, the network will have only tension forces. If decreased, can increase the number of links at each node.

Note. The "Rheological effect" column gives the effect of increasing the parameter on the rheological behavior of the numerical network.

network to variations in stress magnitude. This may make the time-dependent network rules more desirable for implementation in the mechanical modeling of cells. In Fig. 10, we see the qualitatively different effects of the link total age duration t_{tot} on network rheology. Table II summarizes the effects of the time-dependent network parameters on observed rheology.

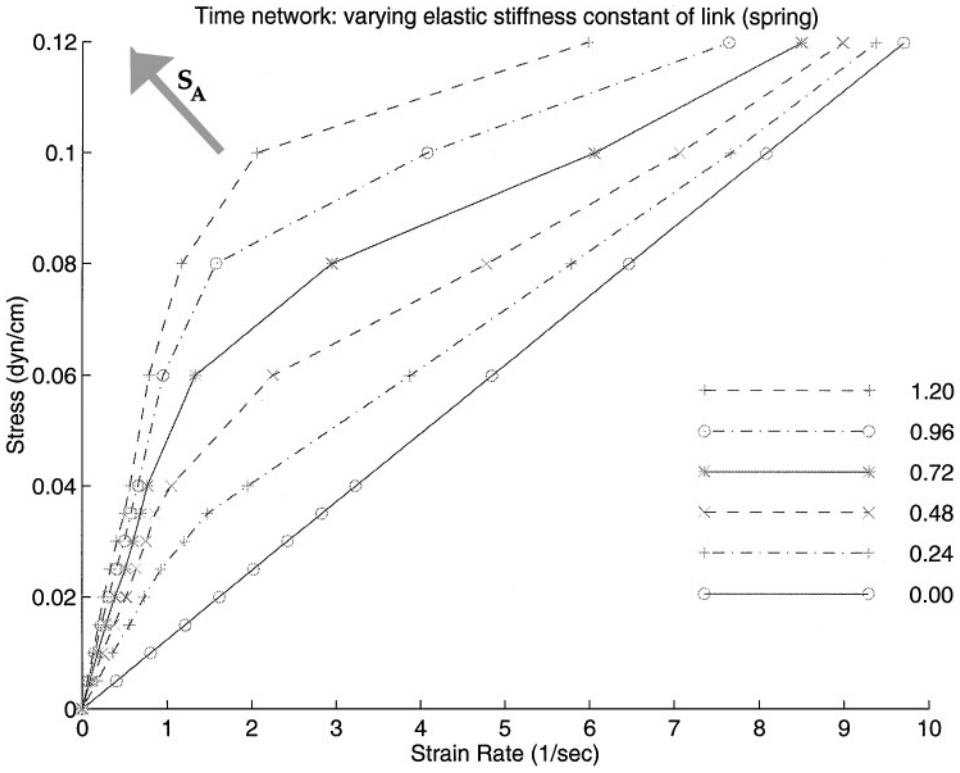

FIG. 9. Stress versus steady-state strain rate curves for time-dependent network. The steady-state viscosity of the network was tested for different values of the elastic link stiffness constant S_A, given in dynes.

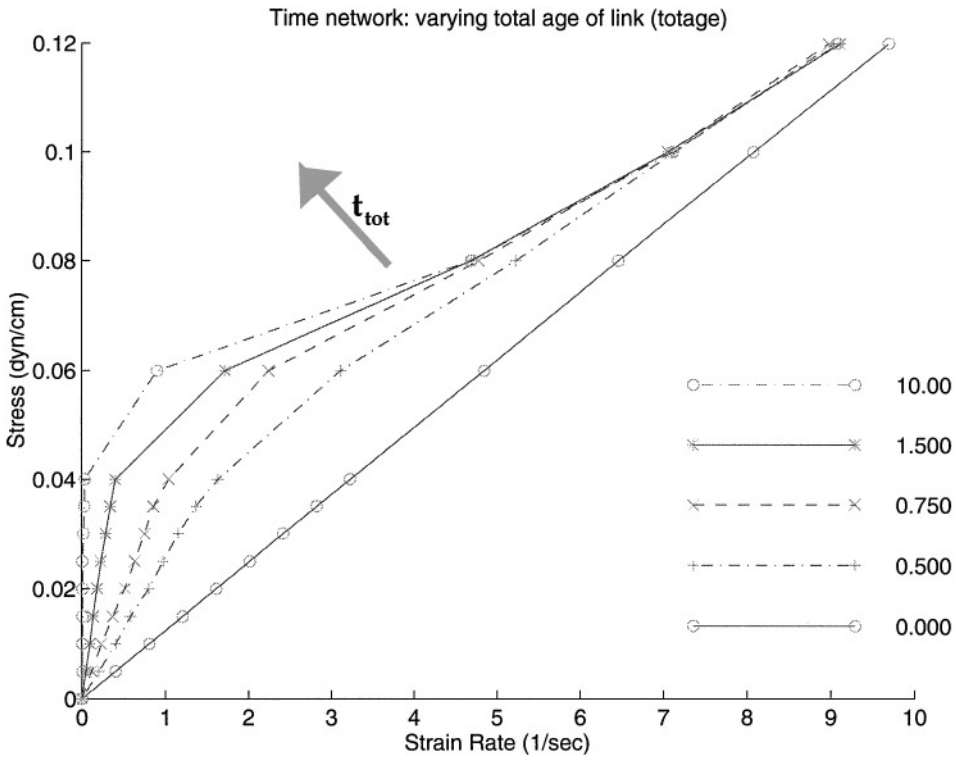

FIG. 10. Stress versus steady-state strain rate curves for time-dependent network. The steady-state viscosity of the network was tested for different values of t_{tot}, given in seconds.

4.1.4. *Stress Overshoot*

Up to this point, it would appear that the "capture-annulus" and time-dependent network rules exhibit roughly the same mechanical behavior. Both act like a viscoelastic fluid under shear stress, and both exhibit shear thinning when subjected to increasing stresses. The capture-annulus rules, however, model a network that reforms instantaneously when the shear stress is removed, whereas *in vitro* actin gels appear to reform with a resistance to strain that increases with the square root of the time after removal of stress, an effect referred to as thixotropy [15]. The time-dependent rules were devised in order to reproduce this *in vitro* behavior.

To test if thixotropy is indeed observed in the numerical "time" network and not in the "capture-annulus" network, the following numerical experiment was devised using the same geometric setup as the previous tests. After an unstressed initialization period of one second, the numerical network was subjected to a stress of 0.08 dyn/cm, sufficient to rupture the network, for a duration of 3 s. After a period of t_{rest} seconds of "rest," a shearing force of 0.04 dyn/cm was once more applied to the network. The mean strain rate over the first second of re-stress was then observed.

The results of these tests are shown in Fig. 11. As expected, the capture-annulus network exhibits the same behavior regardless of rest time. The time-dependent network, however, becomes more resistant to strain the longer it has been allowed to "rest" and reform. Figure 12 shows the effective viscosity μ_e of the time-dependent network as a function of rest time t_{rest}. In this figure we see that, although the experimentally observed $\mu_e \sim \sqrt{t_{\text{rest}}}$ relationship

TABLE II
Numerical Parameters for the Time-Dependent Linking Rules

Parameter name	Default value	Rheological effect	Description and biological interpretation
S_A	0.48 dyn/cm	Stiffening	Stiffness constant; the aggregate stiffness of the actin filaments joining two islands of crosslinked actin.
$r_{\max}$	1.8	Stiffening	outer capture radius ratio; if set equal to 1, the network will have only compressive forces. If increased, increases number of links at each node.
$r_{\min}$	0.8	Relaxing	Inner capture radius ratio; if set equal to 1, the network will have only tension forces. If decreased, can increase the number of links at each node.
r_{rupt}	1.2	Stiffening	The strain ratio at which a link joining two islands ruptures. The stress vs. strain rate curve for $r_{rupt} = 1.0$ is not the same as the curve for $r_{rupt} = 0.0$ (simple fluid), indicating that compressive forces also play a role in the mechanical behavior of the network.
t_{form}	0.25 sec	Relaxing	Link formation time; corresponds to the length of time required for actin network to form between two existing islands of crosslinked actin.
t_{tot}	0.75 sec	Stiffening	Total age of links (including t_{form}) before rupture. Intended to correspond to the constant remodeling of cytoskeleton.

Note. The "Rheological effect" column gives the effect of increasing the parameter on the behavior of the numerical network.

between effective viscosity and rest time does not appear in the numerical simulation, the effective viscosity of the time-dependent network does increase with rest time. The time-dependent network fails to exhibit the $\mu_e \sim \sqrt{t_{\text{rest}}}$ behavior because of the deterministic nature of the link formation rules. It is evident from Fig. 12 that the effective viscosity of the network increases significantly as t_{rest} approaches the link formation time t_{form}, resulting in a greater number of network links and, consequently, a higher effective viscosity. Linking rules involving a stochastic component may be able to better simulate the desired relationship between t_{rest} and μ_e, but this would be at the computational expense of a call to a random number generator for each node–node interaction. To summarize, while the time-dependent network does not reproduce the experimentally observed functional relationship between μ_e and t_{rest}, it provides a qualitative improvement over the time-independent "capture annulus" rules.

4.1.5. *Convergence of Numerical Scheme and Estimate of Computational Expense*

Although there is no formal proof for the convergence of the immersed boundary method in more than one space dimension, we can test empirically for numerical convergence by successively refining the resolution for a fixed test run. If the norm of the difference between numerical solutions of successive refinement decreases with the level of refinement, this can be taken as evidence that the sequence of increasingly refined numerical solutions forms a Cauchy sequence that converges to some solution. A convergence study of this type was conducted in [4] and linear convergence of the method was observed. These studies measured the convergence of the **control**, **memory**, and **capture annulus** networks to

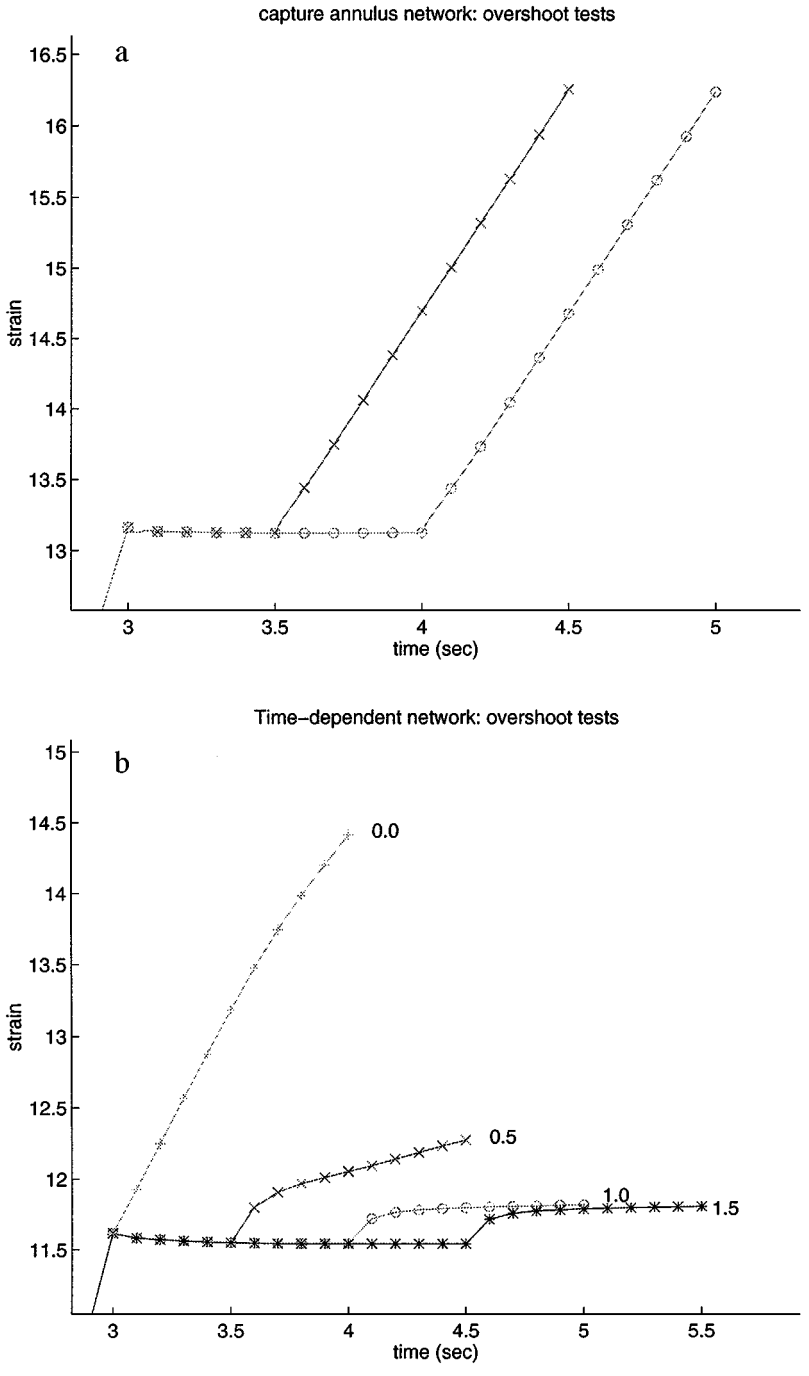

FIG. 11. Evolution of strain resistance in ruptured numerical networks. Note that the capture annulus network (a) seems to retain no information of how long it has been resting; the strain rates are independent of rest time. In the time-dependent network (b), however, the longer the rest time, the more resistant to strain the network is when stress is reapplied. Shown are the strain curves of the material after $t_{\text{rest}} = 0.5$ and 1.0 s of rest (a) and after $t_{\text{rest}} = 0.0$, 0.5, 1.0, and 1.5 s of rest (b).

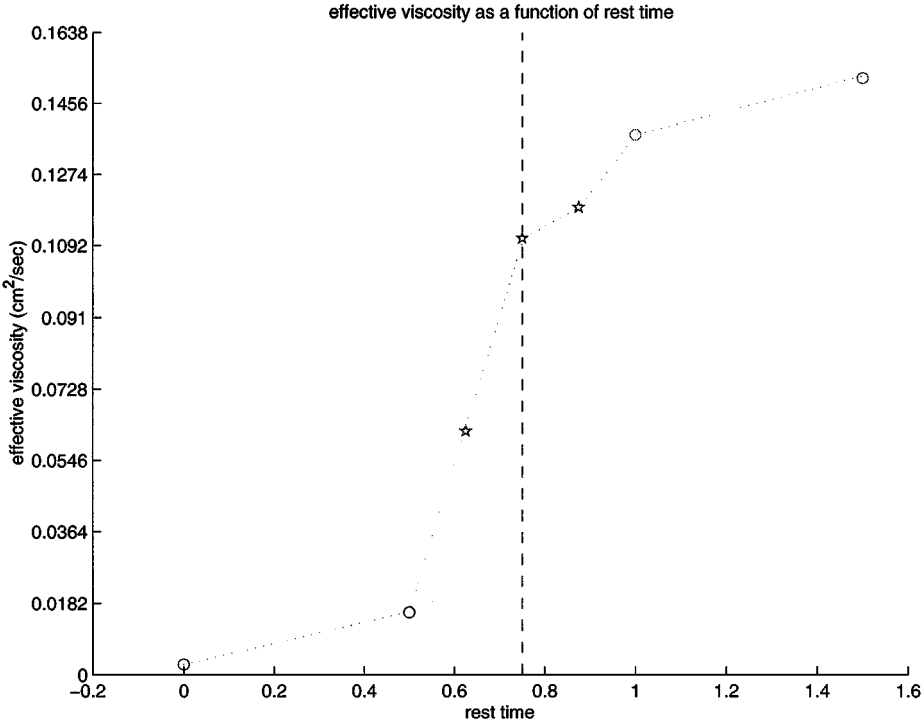

FIG. 12. Relationship between rest time t_{rest} and effective viscosity μ_e in time-dependent network. The effective viscosity was determined by measuring the mean strain rate exhibited by the network over the initial second following reapplication of shear force. The dashed vertical line indicates the formation time $t_{\text{form}} = 0.75$ s, at which point there is an increase in the number of elastic links and, therefore, in the effective viscosity of the network.

creep deformation behaviors of the type shown in Fig. 7. Since the most complex behavior consistently observed for the **time-dependent** network is shear-thinning, more recent convergence studies have been directed toward demonstrating the numerical convergence of this network to a specific stress versus strain rate relationship. Figure 13 and Table III provide evidence that the time-dependent network exhibits linear convergence in stress versus strain rate behavior.

A typical wall shearing run using a 64×64 fluid lattice and a total of 600 actin nodes required approximately 36 min of computational time per second of simulated physical

TABLE III
Convergence Study of Strain Rate $\dot{\epsilon}$ as a Function of Applied Stress in the Time-Dependent Network

Norm →	L_1	L_2	L_∞
$\|\dot{\epsilon}_{32} - \dot{\epsilon}_{64}\| / \|\dot{\epsilon}_{64}\|$	0.0742	0.0072	0.0914
$\|\dot{\epsilon}_{64} - \dot{\epsilon}_{128}\| / \|\dot{\epsilon}_{128}\|$	0.0368	0.0023	0.0532
Convergence ratio	**0.4968**	**0.3135**	**0.5827**

Note. The subscripts of $\dot{\epsilon}$ denote N_G, the number of fluid grid lattice points used. The convergence ratios indicate that the shear thinning behavior of the network converges linearly with increased spatial resolution.

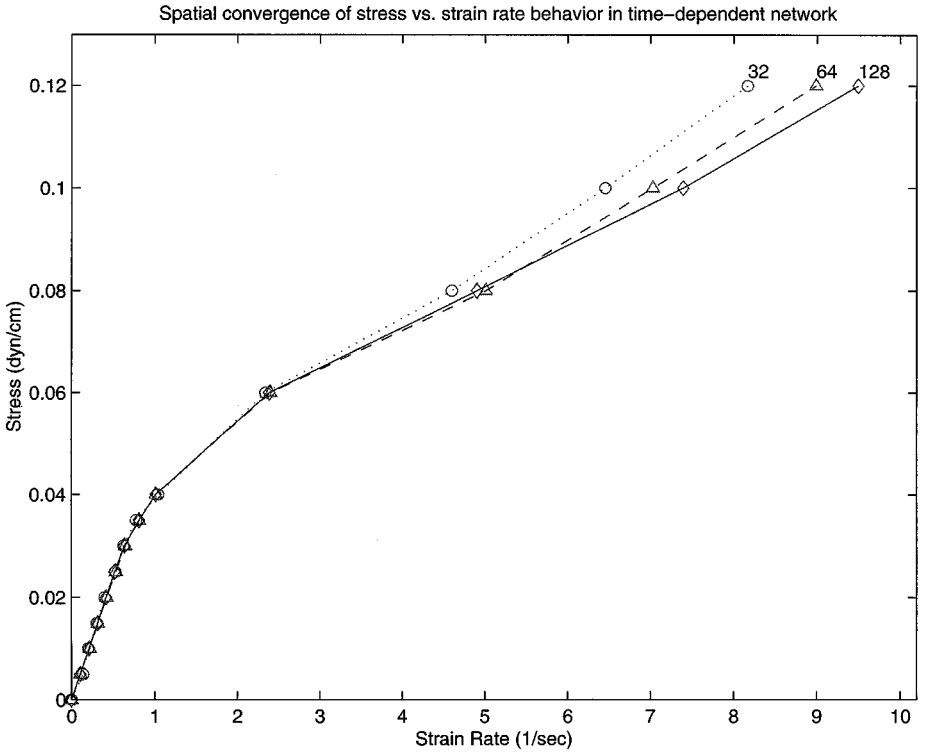

FIG. 13. Numerical convergence of wall shearing simulations under time-dependent linking rules. Shown is the stress versus strain rate behavior of the test network for successive fluid grid refinements of 32×32, 64×64, and 128×128 lattice points.

time running on a single DEC Alpha 2100-5/250 processor. A similar run on a 128×128 fluid lattice with 2200 actin nodes required approximately 156 min of computational time per second of simulated time.

4.2. Micropipette Aspiration Simulations

Numerical simulations modeled after the *in vivo* micropipette aspiration experiments [22, 6, 10, 23] may reveal the aggregate mechanical properties of the model cell, as well as the individual properties of the cell membrane and the actin cytoskeleton under various linking and forcing rules. Although the ultimate goal of this research is to simulate ameboid locomotion, there are several advantages to first simulating biological experiments such as micropipette aspiration. First of all, the biological experiments provide better-defined quantitative and qualitative information to which the numerical results can be compared. Second, the numerical experiments provide an environment in which it is easier to measure the effects of numerical parameters on the passive mechanical behavior of individual cell components as well as the effects of these components on the entire model cell.

4.2.1. *Setup of Model Cell and Numerical Apparatus*

The model cell is initially circular in shape, with radius r_c. The cell membrane is modeled as an impermeable immersed boundary loop $\{\mathbf{M}(s, t)\}$ for $s \in [0, 2\pi r_c]$. Initially, $\mathbf{M}(s, 0)$

TABLE IV
Default Parameter Values Used in Wall Shearing and Micropipette Aspiration Simulations

Parameter	Description	Value
Δt	Timestep	0.0001–0.00025 s
L	Length of square fluid domain	0.0025 cm
N_G	Number of finite-difference grid spaces in fluid domain ($\Delta x = L/N_G$)	64
δA	Interior actin spacing parameter	$2\Delta x$
$\delta A'$	Membrane-embedded actin anchor spacing parameter	$\frac{\Delta x}{2}$
μ	Viscosity of immersing fluid	0.01138 cm^2/s
ρ	Density of immersing fluid	1 g/cm^2
S_M	Membrane stiffness constant	4×10^{-5} dyn
$S_{A\text{-}cyto}$	Stiffness of cytoplasmic (interior) actin links	0.48 dyn/cm
$S_{A\text{-}anchor}$	Stiffness of fibers linking interior actin points to the membrane-embedded actin anchors	$0.1S_{A\text{-cyto}}$

Note. The dimensions of the fluid density and subsequent parameters differ from the dimensions of their physical counterparts by a factor of length^{-1}; this is due to the fact that the simulations were carried out in two dimensions.

describes a circle of radius r_c and the numerical actin network fills the interior of the circle, with the outermost actin nodes acting as anchors embedded in the membrane.[1] At any time t the local dimensionless strain $e(s)$ at a point on the membrane is given by $e(s) = \|\partial \mathbf{M}/\partial s\| - 1$. Studies involving human neutrophils indicate that ameboid cells have up to 137% excess membrane area relative to what they would need to enclose their volume in a sphere [6]. As a result, the membrane unfolds with little or no resistance up to its maximum area, at which point it strongly resists further increases in area. If we think of the length of $\{\mathbf{M}(s, t)\}$ in our two-dimensional model as the "effective area" of the membrane, folding included, we would like $\{\mathbf{M}(s, t)\}$ to stretch easily up to, say, twice its original length (corresponding locally to $e(s) = 1$) before becoming strongly inextensible. Therefore, instead of a Hookean stress–strain relationship for the membrane, we chose one of the form $T(s) = S_M e(s)(10\hat{}(e(s)^{\gamma}))$.[2] The tension stress-strain relationships for the cases $\gamma = 0$ (Hooke's law) and $\gamma = 9$ (used in these simulations) are compared in Fig. 14.

[1] In living cells, the actin cytoskeleton is thought to largely occupy the cortical region immediately beneath the cell membrane. For the purpose of this two-dimensional simulation the contributions of the network mechanics to the mechanics of the entire model cell are more significant if the numerical network is distributed throughout the cell, with a disproportionate density of membrane-embedded actin nodes in order to increase the amount of elastic fibers beneath the model membrane.

[2] This functional form was chosen arbitrarily because it had the desired property of a rapid transition from weak compression to strong tension. Although it may be possible to use statistical mechanics to derive from first principles a functional form for T, such an improvement would be unlikely to have a significant impact on these simulations.

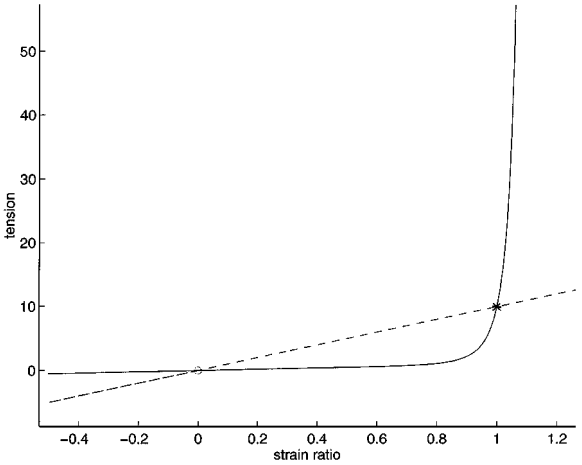

FIG. 14. Comparison of Hookean (dashed line) and nonlinear (solid curve) stress-strain relationships. The membrane is relaxed at its initial configuration for the Hookean ($\gamma = 0$) rule as well as for the nonlinear ($\gamma = 9$) forcing rule. When the membrane is compressed (negative strain ratio), the Hookean forcing would cause the membrane to resist linearly, while the nonlinear forcing would allow the membrane to "fold" easily. For strain ratios up to 1, the nonlinear forcing rule provides little resistance, corresponding to membrane unfolding. At local doubling of length (marked by an asterisk), the nonlinear forcing scheme begins to strongly resist any further lengthening, thereby modeling a taut membrane.

The force density $\mathbf{f}_M$ along the membrane is given by

$$\mathbf{f}_M = \frac{\partial}{\partial s}(T\boldsymbol{\tau}), \tag{21}$$

where $T = T(s)$ is the tension and $\boldsymbol{\tau} = \boldsymbol{\tau}(s)$ is the unit tangent vector to $\{\mathbf{M}\}$ at the point $\mathbf{M}(s, t)$ [20].

The membrane $\{\mathbf{M}(s, t)\}$ is discretized as a loop of points $\{\mathbf{M}_i\}$ with an initial spacing of $\Delta s = \Delta x/4$, where Δx is the finite difference fluid grid spacing introduced in Section 3. This initial spacing is chosen so that when the membrane is stretched tautly, the spacing will be doubled; this maximum spacing of $\Delta x/2$ has been observed in numerical experiments to be sufficient to maintain the impermeability of the model membrane to normal fluid flow. The discretization of (21) at each point $\mathbf{M}_i$ is

$$\mathbf{f}_i = \frac{1}{\Delta s}\left(T_{i+1/2}\frac{\mathbf{M}_{i+1} - \mathbf{M}_i}{\|\mathbf{M}_{i+1} - \mathbf{M}_i\|} + T_{i-1/2}\frac{\mathbf{M}_{i-1} - \mathbf{M}_i}{\|\mathbf{M}_{i-1} - \mathbf{M}_i\|}\right), \tag{22}$$

where $T_{i+1/2}$ gives the tension between the points $\mathbf{M}_i$ and $\mathbf{M}_{i+1}$. In a similar manner to (17), these forces are spread to the fluid grid via

$$\mathbf{F}_{kl} = \sum_i \mathbf{f}_i d(x_i - k\Delta x)d(y_i - l\Delta x)\Delta s. \tag{23}$$

The movement of membrane points in the simulation must be handled differently than other immersed boundary points in order to properly model the cell membrane's unique mechanical properties. In particular, the high diffusivity of membrane phospholipids is believed to allow the integral membrane proteins which bind internal actin filaments to slide freely in the plane of the membrane. As a result, several previous models of ameboid

cell motion have considered a no-penetration, free-slip condition for the interface between the actin cytoskeleton and the plasma membrane [2, 7, 8]. In order to satisfy this interface condition, we update the membrane points $\{\mathbf{M}_i^n\}$ as follows. At each timestep,

1. In a similar manner to the immersed actin nodes in (15), the points $\{\mathbf{M}_i\}$ are moved at the local fluid velocity according to

$$\mathbf{M}_i^{n+1/2} = \mathbf{M}_i^n + \Delta t \sum_{k,l} u_{kl}^n d\left(x_i^n - k\Delta x\right) d\left(y_i^n - l\Delta x\right)(\Delta x)^2. \tag{24}$$

2. A periodic cubic spline is then interpolated through the points $\{\mathbf{M}_i^{n+1/2}\}$, and the points are redistributed evenly along the spline to obtain $\{\mathbf{M}_i^{n+1}\}$.

Therefore the curve described by the membrane moves at the local fluid velocity, but the points inside the curve are being continually redistributed. As a result, the local tension is constant throughout the membrane. More importantly, the actin network nodes originally embedded in the model membrane remain embedded, but the model membrane slips freely past these nodes in the tangential direction.

The numerical apparatus for micropipette aspiration, shown in Fig. 15, consists of the passive model cell and a rigid pipette. The pipette, composed of a neck and a bulb, is tethered to fixed points in space and is also supported throughout by a series of "buttresses," or crosslinks among its immersed boundary points. The pressure drop Δp across the opening of the pipette is established by way of a mass sink inside the micropipette bulb and a source outside the pipette. The support of the source and the sink, on which the Navier–Stokes momentum balance equation (1) is no longer valid, is chosen to be as far away as possible

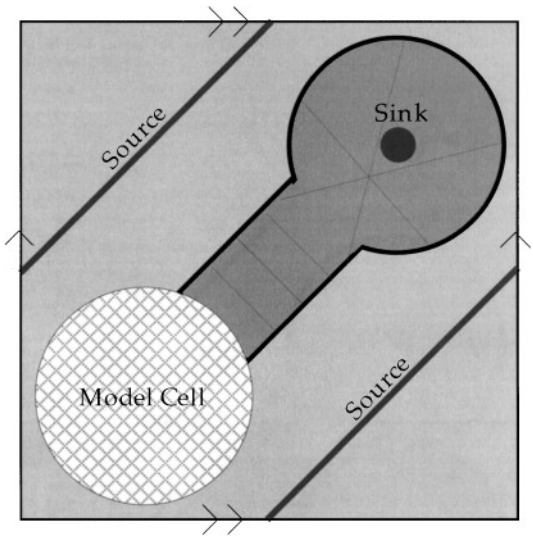

FIG. 15. Initial configuration of numerical apparatus for micropipette aspiration simulations. The source along the indicated diagonal line and the sink in the middle of the pipette bulb work together in order to conserve mass and to establish the target pressure drop. For the purpose of illustration, only a few of the crosslinks that maintain the rigidity of the pipette are shown. The simulated domain is 25 μm across. The pipette diameter is approximately 10 μm across, the typical speed of the aspirated tip is 1 μm/s, and the effective viscosity of the model cytoplasm ranges from 0.01138 cm^2/s to an order of magnitude higher. Thus the Reynolds numbers for these simulations—and their experimental counterparts—range from 10^{-5} to 10^{-6}.

from the immersed structures and therefore from the dynamics of interest. The details of how the pressure drop is established and maintained are given in [4]. In order to determine the effects of the periodicity of the fluid domain on the behavior of the numerical apparatus, two test runs were compared. In the first, the standard setup was used, in which the pipette and model cell apparatus nearly completely occupies the 25 μm^2 64×64 node fluid domain. In the second, a 128×128 node fluid domain twice as large (50 μm across) was used for the same size apparatus. The deformation distance $d(t)$ of the cell into the pipette during suction and release was compared in the two runs, and the maximum difference in $d(t)$ in the two runs was found to be less than 0.5%. It is evident from these tests that the effects of periodicity on the output of these numerical simulations are negligible. All of the simulations that follow were conducted using the 64×64 node 25 μm fluid grid.

4.2.2. *Effects of Model Cell Components on Behavior of Entire Cell*

Micropipette aspiration was simulated in model cells with various mechanical properties. The first tested cell, called the **control** cell, consisted of a fluid-filled, membrane-bound vesicle, but all of the cell's internal forces were set to zero. Mechanically, this was simply a simulation in which a ring of fluid markers was drawn into the pipette. The second test cell was the **membrane** cell, in which the membrane dynamics of nonlinear forcing and spline reinterpolation were in effect but the interior of the cell consisted only of the immersing fluid. The **memory** cell had the membrane forcing rules in effect, as well as the memory network rules (see Section 2) governing the mechanics of the cell interior. The **annulus** cell and the **time** cell also had the membrane forcing activated, as well as the capture annulus and time-dependent network rules, respectively, governing the cytoskeletal linking dynamics in these test cells.

The micropipette aspiration simulations began with a 4-s loading phase, in which a simulated pressure drop, Δp, measured from the exterior environment to the pipette bulb was immediately established and maintained for 4 s. In the unloading phase, the simulated pressure was quickly equilibrated and the model cell was allowed to rebound from its strained configuration. Figure 16 provides a qualitative comparison of the effects of the different model cell components on the aggregate passive mechanical behavior of the simulated cell.

A more quantitative analysis can be made by measuring the deformation distance $d(t)$ of the model cell's protrusion into the pipette neck as a function of time. In experimental studies this one-dimensional quantity is often used to describe the three-dimensional process of cell deformation into the pipette since the creep behavior of a viscoelastic sphere under small deformations is proportional to the creep behavior of a one-dimensional viscoelastic solid [22]. The results of these measurements are shown in Fig. 17. The control cell's strain history is exactly what one would expect of unrestricted fluid flow into the pipette. The membrane cell, since its membrane satisfies a free-slip boundary condition at the pipette wall and, since its initial configuration is at half of its maximum strain, provides very little resistance to micropipette suction. Upon unloading, the membrane cell rebounds slightly, apparently in an attempt to equilibrate membrane curvature from a parabolic shape to a more circular shape.

In the memory, annulus, and time cells, the membrane-embedded actin nodes satisfy a no-slip condition at the pipette opening, but the membrane again satisfies a free-slip condition, both relative to the pipette walls and to the membrane-embedded actin nodes. In all

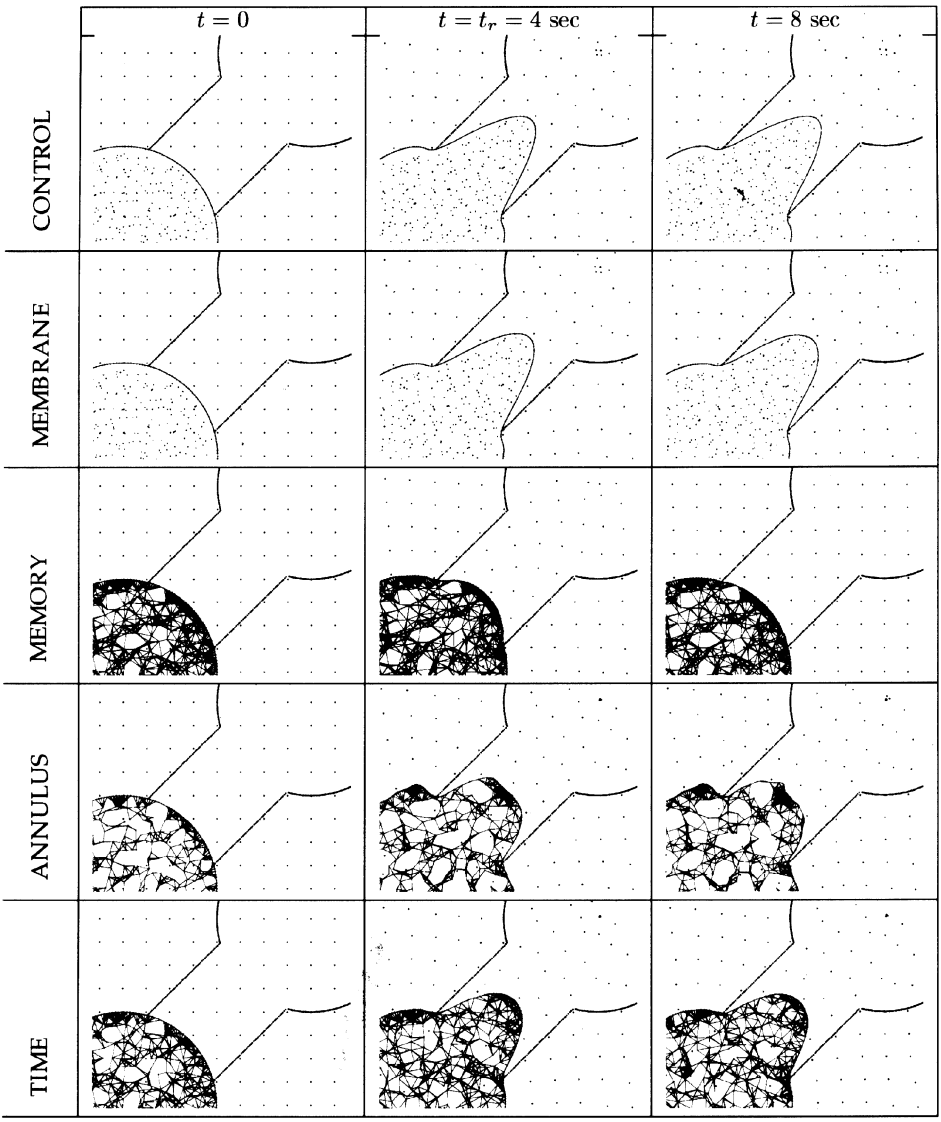

FIG. 16. Comparison of model cell mechanical components in the context of micropipette aspiration simulations.

three simulations we see that the numerical actin network inhibits flow of the cell protrusion into the pipette. The memory cell behaves as the memory network did in the wall shear tests; it strongly resists deformation and rebounds exponentially toward its original circular shape in the manner of a Voigt solid. The annulus and time cells behave similarly to each other. Note, however, that the time cell deforms more than the annulus cell, while the time network in the wall-shearing experiments shown in Fig. 7 deforms *less* than the annulus network. This is because the micropipette aspiration simulation lasts four times longer in simulated time than the wall shearing test. The time network that comprises the interior of the time cell has a total link age t_{tot} on the order of 1 s, so the turnover of the links is manifested as a more fluid-like behavior on longer timescales. Indeed, in the first 2 s of

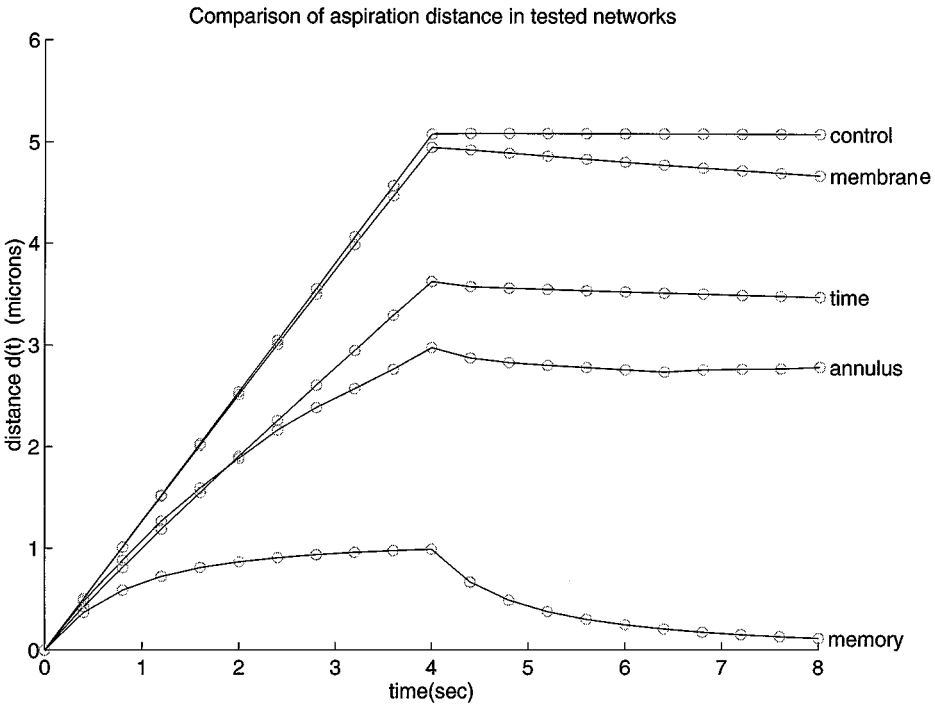

FIG. 17. Aspiration distance plots for various membrane and network linking and forcing rules. Note that the curves interpolated though the numerical data points are not fitted curves but rather have been added for data visualization purposes.

simulated time, the time cell deforms *less* than the annulus cell, but then the two strain histories intersect and thereafter the time network is less resistant to stress.

It should be noted that the model cell does not rebound linearly to a circular shape upon equilibration of pressure. The linear rebound observed in living cells is believed to be due to active contractions in the actin cortex [10]. The viscoelastic network model presented here does not yet include these actomyosin contractions.

4.2.3. *Shear Thinning*

In preliminary simulations of micropipette aspiration over a range of aspiration pressures from $\Delta p = 0.05$ to $\Delta p = 0.20$ dyn/cm, the model cell cytoskeleton did not exhibit shear thinning behavior. Experimentally, the logarithm of cell cytoplasmic viscosity decreases linearly with the logarithm of mean shear rate experienced by the cell protrusion as it is drawn into the pipette [23]. One possible reason that this experimentally observed relationship did not appear is presented in Fig. 18, in which the logarithm of the effective viscosity of the time-dependent network is plotted against the strain rate experienced by the network. The data were obtained from the wall shearing tests in Section 4.1. It is evident from the figure that for lower strain rates, the effective viscosity of the model network remains relatively constant, but for higher strain rates the network enters a regime in which the logarithm of its effective viscosity does decrease linearly with increasing strain rate. Whether the rheology exhibited by the aspired model cell would enter such a regime under higher strain rates has not yet been tested.

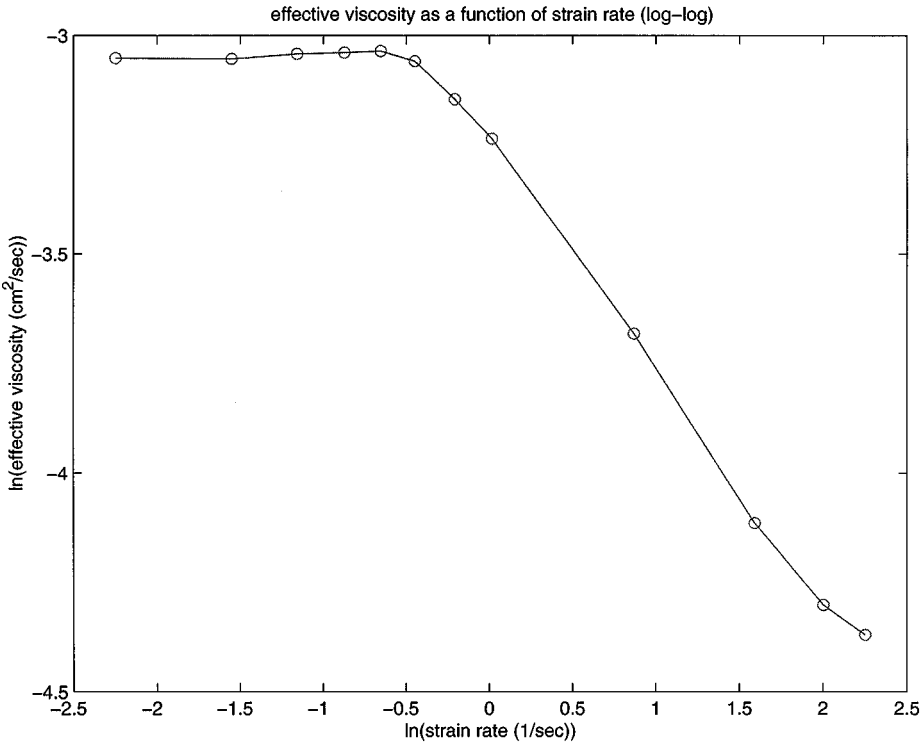

FIG. 18. A log–log plot of the relationship between strain rate and effective viscosity from the wall-shearing test of the time-dependent network. For low strain rates, the network effective viscosity remains relatively constant, but for higher strain rates $\ln(\mu_e)$ decreases linearly with $\ln(\dot{\epsilon})$.

5. DISCUSSION

We have presented a method for modeling passive viscoelastic networks in the context of the immersed boundary method. As we saw in Section 4.1, the network with the memory linking rules behaved like a simple Voigt solid while the capture-annulus and time-dependent networks behaved mechanically like viscoelastic fluids. As shown in Section 4.1.3, the time-dependent and capture-annulus networks exhibit shear thinning behavior when exposed to increasing shear rates. Only the time-dependent network exhibited behavior resembling thixotropy; when ruptured, the effective viscosity of the network would increase the longer the network remained unstressed. The micropipette aspiration simulations in Section 4.2 demonstrated the utility of the model network in the context of modeling passive ameboid cells. Once a three-dimensional cell model of this type is developed, simulations of such *in vivo* tests as cell aspiration and cell squashing may be used to validate the model by comparing it to experimental data.

There are two significant advantages provided by this method over simply using a continuum viscoelastic model throughout the computational domain. The first advantage is that the method presented here allows for the possibility of two-phase flow in the model cell interior. For example, if the actin node spacing δA is sufficiently large, the immersing Newtonian fluid will be able to flow relative to the actin network, thereby mimicking the flow of aqueous cytosol relative to the porous cytoskeleton in living cells. Alternatively, the actin nodes could be allowed to slip relative to the immersing fluid, resulting in the same

effect. The second advantage of using this method is the ability to model an extracellular environment that is much less viscous and effectively Newtonian relative to the cell interior, for example, in the case of cell tumbling in a flow chamber, or of a locomoting ameboid cell in an aqueous medium.

Augmented by the technique presented in this paper, the immersed boundary method is now capable of modeling biological problems involving viscoelastic networks. The advantage of the immersed boundary method is that it allows for the modeling of free-boundary biofluid dynamics problems by expressing the objects of interest as flexible, elastic structures immersed in a simple computational fluid domain. Possible applications of this technique include passive cell deformation, such as the tumbling of white blood cells in arteries, active ameboid cell locomotion, for example the extravasation and chemotaxis of phagocytes toward wound sites, and external fluid dynamics, like the beating of cilia in a viscoelastic mucous medium. Refinements of the method currently being considered include the modeling of active actomyosin contraction, two-phase cytoskeletal/cytosolic flow, protrusive force generation via actin polymerization, and brownian motion.

5.1. Additional Material

Animations of some of the wall-shearing runs and micropipette aspiration simulations have been converted to Quicktime™ movies and posted on the World Wide Web at the following location:

`http://www.math.utah.edu/~bottino/research/passive_cyto/passive_cyto.html.`

ACKNOWLEDGEMENTS

I would like to thank my dissertation advisor, Lisa Fauci, for her help both during my graduate studies and during the preparation of this article, Hans Othmer for his careful reading of the manuscript, and Susan Jancart for her continual support. Finally, I would like to thank the Floating Head of Robert Dillon for appearing at those times when I was most in need of technical guidance and literary motivation. The author was supported in part by DOE Grant FG-01-93EW53023.

REFERENCES

1. B. Alberts *et al.*, *Molecular Biology of the Cell*, 3rd ed. (Garland, New York, 1994).
2. W. Alt, Mathematical models and analysing methods for the lamellipodial activity of leukocytes, in *Biomechanics of Active Movement and Deformation* (Springer-Verlag, Berlin, 1990), p. 403.
3. D. R. Bland, *The Theory of Linear Viscoelasticity* (Pergamon, Oxford, 1960).
4. D. C. Bottino, *An Immersed Boundary Model of Ameboid Deformation and Locomotion*, Ph.D. thesis, Tulane University, 1996.
5. D. Bray, *Cell Movements* (Garland, New York, 1992).
6. S. Chien *et al.*, Viscoelastic properties of leukocytes, in *White Cell Mechanics: Basic Science and Clinical Aspects*, edited by H. J. Meiselman, M. A. Lichtman, and P. L. LaCelle (A. R. Liss, New York, 1984), p. 19.
7. M. Dembo, Field theories of the cytoplasm, *Comments Theoret. Biol.* **1**, 59 (1989).
8. M. Dembo and F. Harlow, Cell motion, contractile networks, and the physics of interpenetrating reactive flow, *Biophys. J.* **50**, 109 (1986).

9. R. Dillon, L. Fauci, A. Fogelson, and D. Gaver, Modeling biofilm processes using the immersed boundary method, *J. Comput. Phys.* **129**, 57 (1996).
10. E. A. Evans, Structural model for passive granulocyte behaviour based on mechanical deformation and recovery after deformation tests, in *White Cell Mechanics: Basic Science and Clinical Aspects*, edited by H. J. Meiselman, M. A. Lichtman, and P. L. LaCelle (A. R. Liss, New York, 1984), p. 53.
11. L. J. Fauci, Interaction of oscillating filaments: A computational study, *J. Comput. Phys.* **86**(2), 294 (1990).
12. L. J. Fauci and C. S. Peskin, A computational model of aquatic animal locomotion, *J. Comput. Phys.* **77**(1), 85 (1988).
13. A. L. Fogelson and L. J. Fauci, Truncated newton methods and the modeling of complex immersed elastic structures, *Commun. Pure Appl. Math.* **46**, 787 (1993).
14. Y. C. Fung, *Biomechanics: Mechanical Properties of Living Tissues* (Springer-Verlag, Berlin, 1981).
15. P. A. Janmey, Mechanical properties of cytoskeletal polymers, *Current Opinion Cell Biol.* **2**, 4 (1991).
16. J. M. Lackie, *Cell Movement and Behaviour* (Allen & Unwin, London, 1986).
17. C. S. Peskin, Numerical analysis of blood flow in the heart, *J. Comput. Phys.* **25**(3), 220 (1977).
18. C. S. Peskin and D. M. McQueen, A uniform finite difference grid Navier–Stokes solver, unpublished.
19. C. S. Peskin and D. M. McQueen, A general method for the computer simulation of biological systems interacting with fluids, in *SEB Symposium on Biological Fluid Dynamics, July 1994*.
20. C. S. Peskin and D. M. McQueen, A three-dimensional computational method for blood flow in the heart. I. Immersed elastic fibers in a viscous incompressible fluid, *J. Comput. Phys.* **81**, 372 (1989).
21. W. H. Press *et al., Numerical Recipes: The Art of Scientific Computing (FORTRAN Version)* (Cambridge Univ. Press, Cambridge, 1989).
22. R. Skalak, S. Chien, and G. W. Schmid-Schönbein, Viscoelastic deformation of white cells: Theory and analysis, in *White Cell Mechanics: Basic Science and Clinical Aspects*, edited by H. J. Meiselman, M. A. Lichtman, and P. L. LaCelle (A. R. Liss, New York, 1984), p. 3.
23. R. E. Waugh and M. A. Tsai, Shear rate-dependence of leukocyte cytoplasmic viscosity, in *Cell Mechanics and Cellular Engineering* (Springer-Verlag, New York/Berlin, 1994), p. 33.